Particuology 116 (2026) 437–447

Contents lists available at ScienceDirect

Particuology

journal homepage: www.elsevier.com/locate/partic

Effective thermal conductivity of packed bed of porous biochar particles

Nicole Vorhauer-Huget[a,1], Zahra Ghasemi Monfared[b,1], Neda Kazemi[a], Eduardo Arango Durango[b], Evangelos Tsotsas[a], Kentaro Umeki[b,*]

[a] Otto von Guericke University Magdeburg, Thermal Process Engineering, Universitätsplatz 2, 39106, Magdeburg, Germany
[b] Luleå University of Technology, Division of Energy Science, Laboratorievägen 14, 971 87, Luleå, Sweden

HIGHLIGHTS

- Densified biochar particles with various particle size and packed bed porosity.
- X-ray tomography used to access the particle structure.
- Assessment of experimental data with a modified Zehner-Bauer-Schlünder model.
- Dispersed biochar particles appeared to have no significant thermal contact.
- Effective thermal conductivity as a function of particle size and packed bed porosity.

GRAPHICAL ABSTRACT

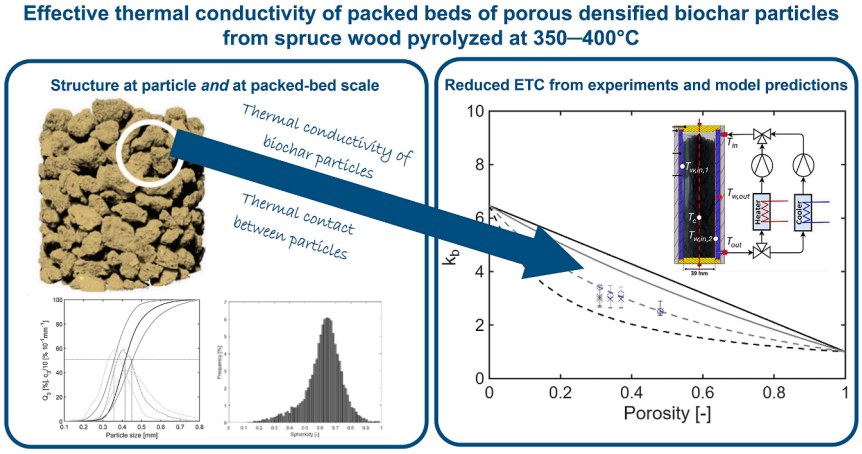

ARTICLE INFO

Keywords:
Experimental determination of ETC
ZBS model
Particle geometry
X-ray tomography

ABSTRACT

In metallurgical processes, packed beds of biochar are subjected to thermal gradients and heterogeneous reactions. In addition, densified biochar particles emerge as a promising carbon-negative insulation solution for building constructions. This makes the effective thermal conductivity (ETC) a critical parameter, but the ETC of biochar particles has not been systematically investigated in dependence of particle size, shape and packed bed porosity. This work aims to partially fill this gap by using densified biochar from spruce bark. The ETC is derived from experiments under non-reactive conditions and numerical analysis including the Zehner–Bauer–Schlünder (ZBS) model. X-ray microtomography was used to quantify particle structure, including sphericity and void fraction. Thermal properties were measured experimentally, and ETC was determined for various particle size fractions between 0.315 and 6.3 mm. The smaller particle fractions exhibited similar bed porosities and ETCs, whereas the largest particle fraction (4-6.3 mm) showed slightly lower ETC and higher bed porosity. Analysis with the ZBS model revealed the need to include an additional thermal resistance in the gap between the

This article is part of a special issue entitled: Reactive Particle-Gas Systems II published in Particuology.

* Corresponding author.
E-mail address: kentaro.umeki@ltu.se (K. Umeki).

[1] These authors share the equal first authorship.

https://doi.org/10.1016/j.partic.2026.06.036
Received 27 January 2026; Received in revised form 19 June 2026; Accepted 29 June 2026
Available online 10 July 2026
1674-2001/© 2026 Chinese Society of Particuology and Institute of Process Engineering, Chinese Academy of Sciences. Published by Elsevier B.V. This is an open access article under the CC BY license (http://creativecommons.org/licenses/by/4.0/).

irregular particles due to the imperfect contact of particles. The results highlight the importance of manipulating inter-particle thermal contacts in altering the ETC of packed beds of irregular particles.

1. Introduction

Packed bed reactors (PBRs) consist of randomly packed particles where heat and mass transfer, along with heterogeneous reactions, are strongly influenced by their structure (Rodrigues et al., 2022). This involves particle size distribution, shape, and consequently, contact areas between particles as well porosity of the packed bed and tortuosity. The effective thermal conductivity (ETC) is a key thermophysical property for such PBRs. ETC governs the heat flux by conduction within the bed, making it vital for applications where uniform temperature distribution is aspired, such as in catalytic processes and energy storage systems. Understanding the structural intricacies of packed beds and their influence on thermophysical properties is essential to gain fundamental process understanding and for accurate design and performance prediction.

Temperature gradients exist inside PBRs due to external heating and cooling, as well as exothermic or endothermic phase changes and reactions. The overall rates of heat transfer induced by such gradients can be influenced by:

(1) conduction through the solid particles, conduction across contact points between adjacent particles and conduction through the stagnant gas phase;
(2) advective heat transfer by fluid going through the bed of particles, which can be spatially non-uniform due to turbulent mixing and irregular flow paths; and
(3) thermal radiation between solid surfaces that become significant at temperatures above 500 °C.

The case described in (1) is of special interest for the present work, i.e. heat transfer by stagnant gas and solid (Van Antwerpen et al., 2010). In this case, ETC depends on the bed void fraction (also denoted as bed porosity) as well as contact points and contact areas between particles (Nasr et al., 1994). It is important to note that in fixed packed beds, advective heat transfer is typically negligible due to the low Reynolds numbers characteristic for stagnant or slow-moving gas phases. Under such conditions, heat transfer is dominated by conduction through the solid particles, contact points, and the interstitial gas phase (Tsotsas & Schlünder, 1990).

The ETC of packed beds has traditionally been estimated through a range of empirical and semi-empirical models (Tsotsas & Martin, 1987a). Some of these models use a combination of resistances in series and in parallel (Thunman & Leckner, 2002). The Maxwell-type models give the analytical solution of the ETC at low and high porosities by considering the system as inclusions of small spheres in continuous media (Kiradjiev et al., 2019). Some studies attempted to extend the model for intermediate void fraction where the effect of particle contacts becomes significant (Xu et al., 2016). Kunii and Smith (Kunii & Smith, 1960) introduced the unit cell approach in which thermal resistances in the solid and fluid phases are modeled in parallel and in series configurations. Many researchers have extended and developed the unit cell approach and have introduced analytical expressions for computing the ETC of packed beds (Cheng et al., 1999; Rodrigues et al., 2022; Van Antwerpen et al., 2010; Zehner & Schlünder, 1970).

Among the analytical models employing the unit cell approach, the Zehner-Bauer-Schlünder (ZBS) model stands out, as it incorporates factors such as void fraction, particle shape, and contact area between particles (Tsotsas & Martin, 1987a). This model assumes simultaneous heat transfer through three processes: conduction in the solid phase via contact points between particles, conduction in the gas phase and radiation. Note that the latter has no relevance in this work. The ZBS model and its variants have been widely used to provide approximate values for the ETC of packed beds with spherical and non-spherical particles, with studies such as Qian et al. (2018) and Rodrigues et al. (2023) confirming its agreement with experimental data.

Many studies have focused on idealized particle shapes and regular packing arrangements, often simplifying calculations by assuming spherical particles and uniform densities. However, studies like (Gan et al., 2017; Govender et al., 2020; Hamilton, 1962) have highlighted the critical influence of particle shape on ETC. For instance, Hamilton (1962) experimentally showed that particle shapes deviating from the ideal sphere led to an increase in the ETC of packed beds. On the other hand, Gan et al. (2017) observed that ETC is constant upon sphericity for disc-like ellipsoids but decreases for rod-like ones. In brief, ZBS models consider the effect of the particle shape and offer flexibility by incorporating additional factors that influence thermal conductivity. Examples are the Knudsen effect which becomes significant at low gas pressures or small particle diameters as well as temperature variations through radiation. In addition, imperfections of thermal contact between particles have been incorporated by Rodrigues et al. (2022). The latter is of special relevance for irregularly shaped particles, such as broken biochar, where limited particle contact likely occurs.

Rodrigues et al. (2023) showed that ETC depends on particle shape when the particle conductivity is significantly higher than that of the gas. In contrast, when the particle conductivity is close to that of the gas phase, the ETC of the bed is less sensitive to the particle shape. More importantly, Rodrigues et al. (2022) have shown that thermal conduction between particles depends in both cases, i.e. even for high particle conductivity, not only on particle shape and related contact areas but severely on the thermal connectivity in the contact region between them. When the contact between particles is not perfect, because of e.g. anomalies in the particle packing or even due to high surface roughness, heat transfer can be significantly impaired. This means that at contact points between particles, regardless of the apparent size of the contact surface, heat transfer is a combination of solid-to-solid conductivity and gas conductivity. If the particles are small and the gas pressure low, the Knudsen effect comes additionally into play. However, the latter does not play a role in the case of thermally poorly contacted particle surfaces under the conditions discussed here.

Packed beds of biochar are used in heterogeneous reactions with vast applications, e.g. in metallurgy, and require the prediction of thermal properties for a wide range of bed structure. Heat transfer is in such applications key to process performance and of fundamental importance for process safety, e.g. to avoid thermal runaways during storage and transportation. Of major interest is the variation of ETC of the packed bed with particle sizes, porosity, and particle shape. To the best of our knowledge, literature does not provide data for biochar packed beds with such applications, especially with a distinction of particle and bed properties. In available literature references, either not pyrolyzed biomass from different wood sources is studied or biochar as an additive to solid mixtures, e.g. of soil, clay, PEG, etc. (Bianchi Janetti et al., 2024; Khaledi et al., 2023; Liu et al., 2022; Mason et al., 2016; Osman et al., 2024). To close current gaps of knowledge, we investigate ETC of pyrolyzed spruce bark chips with various particle size fractions between 0.315 and 6.3 mm, exhibiting bed porosities between 31 and 48 %. Particle morphology is studied by non-destructive imaging using X-ray microtomography (XMT) (Gan et al., 2017; Hamilton, 1962; Khaledi et al., 2023; Zehner & Schlünder, 1970).

Even when biochar particles are densified, they are still highly porous and expected to have a significantly lower thermal conductivity than non-porous solid carbon, i.e. yielding a similar situation as observed by Rodrigues et al. (2023) in their study in the region of low

particle conductivity. Since the thermal contact between particles is of significant importance for heat transfer through the packed bed, we combined the ZBS model for non-spherical particles from (Rodrigues et al., 2023) with the model version proposed by Rodrigues et al. (2022) that accounts for contact imperfections between particles to investigate the related effect on a quantitative base. The approach differs from the traditional ZBS model (Tsotsas & Martin, 1987a) in several ways (consideration of particle shape, introduction of an additional thermal resistance at the contact point between particles by a parameter called imperfection factor s^* in Rodrigues et al. (2022). Therefore, the here used version of the ZBS model will be called extended ZBS model and denoted by ZBS-E. Effective thermal conductivities calculated by this model are denoted by ETC^{ZBS-E}.

Experiments, including measurement of particle conductivity and bed conductivity, were conducted and the obtained results are compared to literature models.

The manuscript is organized as follows. At first, materials and experimental methods are described in Section 2, including image analysis by XMT in Section 2.2.; particle size and sphericity determination by XMT and Camsizer measurements in Section 2.3; evaluation of packed bed properties in Section 2.4; measurement of thermal properties in Section 2.5 and description of the experimental setup for ETC in Section 2.6. Section 2.7 summarizes the numerical approaches, including the ZBS-E model. Afterwards, Section 3 collects the results, starting with structural and thermophysical particle properties (Section 3.1), packed bed properties (Section 3.2), followed by numerical assessment of the measured ETC results, which are presented in Section 3.3, in Section 3.4, using literature models and the modified ZBS-E model from Rodrigues et al. (2022).

2. Materials and methods

2.1. Material

Biochar particles in the present study were obtained from the pyrolysis of dried spruce bark chips in a pilot-scale rotary kiln reactor. Although the external flows of heating media inhibit the direct measurement of pyrolysis temperature, a previous modeling study estimated it to be around 350-400 °C with a residence time of ca. 45 min (Babler et al., 2017).

Biochar particles were mixed with a binder and densified with a vacuum extruding process to a cylindrical shape and then crushed into smaller particles to eliminate the anisotropic pore structure and anisotropic thermal conductivity inside individual particles. Afterwards, they were separated into different size classes using the sieving method according to ASTM C136-01. For this purpose, approximately 70 g of biochar sample were placed on a stack of stainless-steel sieves with mesh apertures ranging from 0.18 mm to 7.1 mm, mounted on a mechanical sieve shaker (Retsch AS200). The sieves were shaken to separate the particles by size, and the fractions retained on each sieve were collected after the process. The five fractions used in this study are differentiated based on the mesh apertures given in Table 1.

2.2. X-ray microtomography and image processing

Packed beds of the particle fractions given in Table 1 were studied by X-ray microtomography (XMT), following (Ramandi et al., 2016; Redenbach et al., 2011; Valverde & Wijewickreme, 2024), using Zeiss Xradia 510 Versa. The prepared beds all had an inner diameter of 23 mm and a height of 18 mm (Fig. 1). XMT was performed using an X-ray tube voltage of 40 kV and a tube power of 3 W to reduce beam hardening artifacts. Each scan collected 1601 projections over a full 360° rotation. Image resolutions were adjusted based on the particle sizes, with voxel sizes of 5 μm for packed beds containing smaller particles of around 0.315 mm (MDP1 in the table) and 23 μm for all other samples (MDP2 to MDP5). The number of particles in the samples ranged from about 70 in MDP5 to 200,000 in MDP1.

Table 1
Mesh apertures of the sieves used to extract individual particle fractions studied in this work: d_{min} and d_{max} denote the minimum and maximum particle size.

Sample	d_{min} [mm]	d_{max} [mm]
MDP1	0.315	0.4
MDP2	0.5	0.6
MDP3	1.0	2.0
MDP4	2.0	3.15
MDP5	4.0	6.3

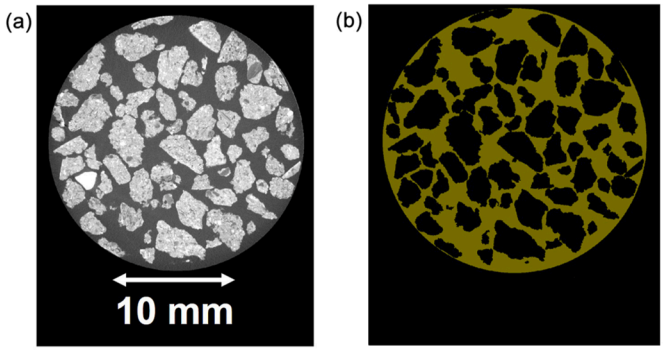

Fig. 1. (a) Raw image from XMT with voxel size 23 μm and (b) binarized segmented image of a cross section of MDP4. Note that the contact points between particles are not likely to be seen in 2D projection.

Image processing was carried out with DRAGONFLY (Version, 2022.2 Build 1367), Comet Technologies Canada Inc. (Object Research Systems). Each stack of grayscale (16-bit TIFF) images underwent segmentation to differentiate solid and inter-particle voids larger than the above-mentioned voxel sizes of 5 and 23 μm. Note that the intra-particle pore space, i.e. internally of the particles, was not resolved with the given local resolution. To accurately separate the particles and the void space, a thresholding method was applied, with manual selection of peaks from a bimodal histogram of grayscale intensity values obtained from Fig. 1(a). Additional refinements were then applied on the segmented regions, including the removal of noise through elimination of disconnected voxel groups smaller than 3 × 3 × 3 voxels as well as filling small holes within segmented particles, which may have resulted from lower intensity values. The result is shown in Fig. 1(b). In the binarized image shown in Fig. 1(b), yellow areas are the void space between the particles (i.e. inter-particulate); the background as well as the solid particles are represented in black. Note that the pores inside the particles (i.e. intra-particulate) are not resolved and the particles appear completely in black in Fig. 1(b).

2.3. Particle size and sphericity

2.3.1. Particle size

The particle fractions summarized in Table 1 were analyzed with a Camsizer from Microtrac Retsch GmbH, Germany. The measurement principle employs a CCD-camera and a very bright LED strobe light source to observe the projection areas of the passing particles that are freely falling in stagnant air. The resolution covers a wide range from 30 μm to 30 mm. Depending on the orientation of the particles in front of the camera, the projected shadow basically varies between the minimum and maximum extension.

The 3D morphology of a representative biochar sample of MDP4 is depicted in Fig. 2. The images were obtained by XMT, following the procedure described in the previous section. But in contrast to Fig. 1(b) the particle is now shown in yellow (and not in black). As can be seen, the particle is rather non-spherical but elongated to one side.

2.3.2. Sphericity

Sphericity describes how closely the particle shape approaches that of a perfect sphere. It ranges from one (perfect sphere) to zero.

The sphericity is an important morphological measure for numerical approaches, where the particle shape affects parameterization of, e.g., heat transfer equations. In this regard, sphericity is relevant for the ZBS-E model, applied in this work to compute the thermal conductivity of the packed bed. As already presented in Fig. 2, the biochar particles have a non-spherical shape with unilateral elongation.

Particle sphericity was determined by two different methods: The volume-based sphericity, ψ_{3D}, was derived from XMT images and the area-based sphericity, ψ_{2D}, often also called circularity, was determined based on Camsizer (Microtrac Retsch GmbH, Germany) measurements.

The 3D volume-based parameter is expressed as:

$$\Psi_{3D} = \frac{\left(6\pi^{1/2}V_p\right)^{2/3}}{A_p}, \tag{1}$$

where V_p and A_p are the volume and surface area of the particle, respectively. In this study, the particle volume was estimated from the number of voxels belonging to a single particle multiplied with the voxel size (5 μm for MDP1 and 23 μm for the rest of the samples). Since the voxel size is less than 2 % (MDP1) and less than 5 % (all other samples) of the median particle diameter, it is assumed that the bias of image binarization during solid and void segregation does not affect accuracy in this step.

The surface area of particles was computed using the DRAGONFLY function based on Lindblad et al. (2002).

The 2D area-based sphericity is defined as:

$$\Psi_{2D} = \frac{4\pi A}{p^2}, \tag{2}$$

with projection area A and perimeter of the projected particle p.

2.4. Packed bed properties

The 3D illustration of an example XMT-scan is given in Fig. 3. The overall bed volume is given by:

$$V_b = \pi r_b^2 h_b, \tag{3}$$

with radius r_b and height h_b of the packed bed.

The particle volume is represented by V_p and integrates the whole envelope volume, thereby ignoring the exact internal particle structure or the presence of intra-particle pore volumes V_{pore}. The volume of the void space between particles can be expressed by the difference $V_b - V_p$. Finally, the solid volume, that is, the volume of solid excluding the intra-particle pore volume from the particle volume, contained inside the packed bed is given by V_s.

The solid density (also referred to as skeleton or true density) can be expressed as:

$$\rho_s = \frac{m_s}{V_s}, \tag{4}$$

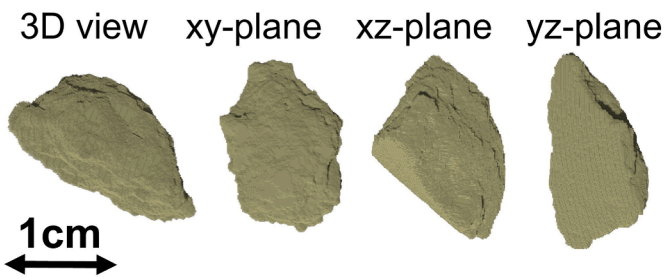

Fig. 2. Selected biochar particle from fraction MDP4.

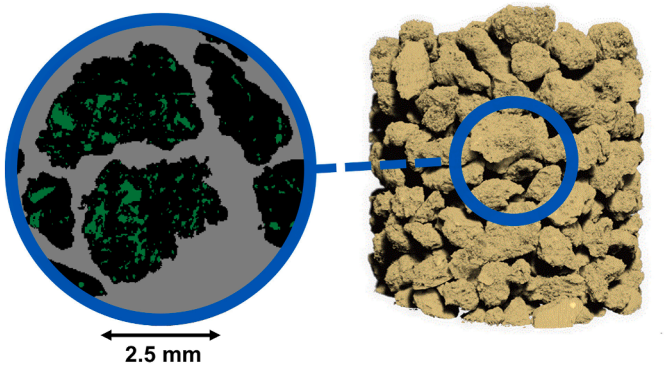

Fig. 3. XMT-based 3D visualization of a packed bed of irregularly shaped particles on the right. On the left is the binarized 2D image of a cross-section of the packed bed. Here, the solid is again represented in black, inter-particle void space is shown in gray, and intra-particle pores that are greater than 23 μm are highlighted in green.

with m_s being the mass of the biochar sample.

The solid volume, V_s, was obtained from helium pycnometry (Ultrapycnometer 1000 version 2.4 from Anton Paar QuantaTec, Austria). This method simply determines the displaced volume of the gas by the solid sample in a pressurized gas chamber. The measurement was conducted with one sample of MDP1 at a temperature of 25 °C and a target pressure of 103,421.4 Pa (15 PSI). Although helium is expected to penetrate into pores in the sub-nanometer range, closed pores are not accessed by this method. Main measurement uncertainties are thus referred to closed pores, which can apparently increase the solid volume during the measurement and result in a lower apparent density for the particle.

The envelope density of a particle is defined as:

$$\rho_p = \frac{m_s}{V_p}. \tag{5}$$

It was estimated from the densified biochar particles before they were crushed into smaller fractions. The particle mass and volume were obtained from the mass and geometrical volume of the vacuum extruded cylindrical pellets.

Finally, the bulk density of the packed bed is defined as

$$\rho_b = \frac{m_s}{V_b}. \tag{6}$$

It can be experimentally estimated simply from the bed geometric volume, V_b, and weight, m_b.

The intra-particle void fraction is derived from the density measurement results:

$$\varepsilon_p = 1 - \frac{\rho_p}{\rho_s}. \tag{7}$$

Similarly, the inter-particle porosity is given by:

$$\varepsilon_b = 1 - \frac{\rho_b}{\rho_p}, \tag{8}$$

with ρ_b from Eq. (6) and ρ_p from the single particle measurements, Eq. (5).

Alternatively, ε_b can also be determined from XMT image data. For this purpose, we have used cross-sectional slices of XMT images cut at 0.02 mm intervals. In more details, the area-averaged porosity is:

$$\varepsilon_b^{2D} = \frac{A_{void}}{A_{\text{sec tion}}}, \tag{9}$$

with A_{void} being the area of void space in each section and $A_{section}$ the total area of each cross-section. Secondly, the volume-averaged bed void

fractions were obtained by averaging all the area-averaged void fractions along the height of the bed:

$$\varepsilon_b^{3D} = \varepsilon_b = \frac{\sum z_{vxl} \cdot A_{void}}{\sum z_{vxl} \cdot A_{\sec tion}}, \tag{10}$$

with z_{vxl} being the height of the slice in terms of voxels. The overall porosity, ε_t, (including both inter- and intra-particle porosities) is finally given as:

$$\varepsilon_t = \varepsilon_p(1-\varepsilon_b) + \varepsilon_b. \tag{11}$$

2.5. Specific heat capacity and thermal conductivity of single particles

The particle thermal conductivity, λ_p, is affected by the intra-particle porosity. It therefore deviates from the (intrinsic) solid conductivity and rather appears as an effective particle conductivity. It can be experimentally obtained using the effective thermal diffusivity of particles (α_p), envelope particle density (ρ_p) and specific heat capacity ($c_{p,p}$) of the porous biochar particles, based on the following equation:

$$\lambda_p = \alpha_p \rho_p c_{p,p}. \tag{12}$$

We used LFA 467HT from NETZSCH GmbH, Germany, and coin-shaped samples with diameters of 12.5 ± 0.2 mm and thicknesses of 2.5 ± 0.5 mm for the measurement of α_p. In order to minimize the experimental error based on light adsorption, a graphite film coating was applied over both the biochar samples and the reference surfaces.

The LFA technique (Light Flash Analysis) was also employed for indirect $c_{p,p}$ measurement through a comparative determination method using the same sample. In this approach, the particles and reference material (pyroceram 9606 from Netzsch GmbH with the diameter of 12.7 mm and the thickness of 1.0 mm) were analyzed sequentially under the same conditions. The $c_{p,p}$ of the porous particles was calculated according to the following equation:

$$c_{p,p} = \frac{T_{ref}}{T_p} \cdot \frac{(\rho l)_{ref}}{(\rho l)_p} \cdot c_{p,ref}, \tag{13}$$

where T is the temperature and l is the thickness of the sample and reference sample. The variation in the density, ρ_p, of the biocarbon with respect to temperature was calculated based on weight changes, assuming a constant volume.

2.6. Effective thermal conductivity (ETC) of packed beds

The setup for the experimental determination of ETC is depicted in Fig. 4 (Rodrigues et al., 2022). The measurement method can be described as transient and radial.

In more detail, the setup includes a copper cylinder with an inner diameter of $D = 39$ mm and a height of $H = 200$ mm. Note that the inner diameter is $D/d_A < 20$ in case of MDP4 to MDP5, i.e. for the particle fractions with larger median diameters d_A. Precisely, $D/d_A \sim 13$ for MDP4 and $D/d_A \sim 8$ for MDP5. This is in the range of values reported in Rodrigues et al. (2022). It could be argued that the wall effect might have a greater impact on the overall packed bed porosity if $D/d_A < 20$, as the wall porosity is usually higher (up to 100 %) in the vertical particle layers along the cylinder wall. This could principally affect ETC measurements, potentially resulting in overall lower ETCs for these configurations. These cases, especially MDP5 could thus be regarded as limits with higher packed bed porosities.

Temperatures are detected at distinct positions as shown in Fig. 4. Temperature in the center of the particle bed is measured by a vertically inserted thermocouple, i.e. axially aligned to the main direction of (radial) heat transfer. This configuration avoids thermal impact of the thermocouple during the transient measurement of center temperature. Insulating disks at the top and bottom, as well as insulation wool at the outer surface of the cylinder ensure that the system is thermally

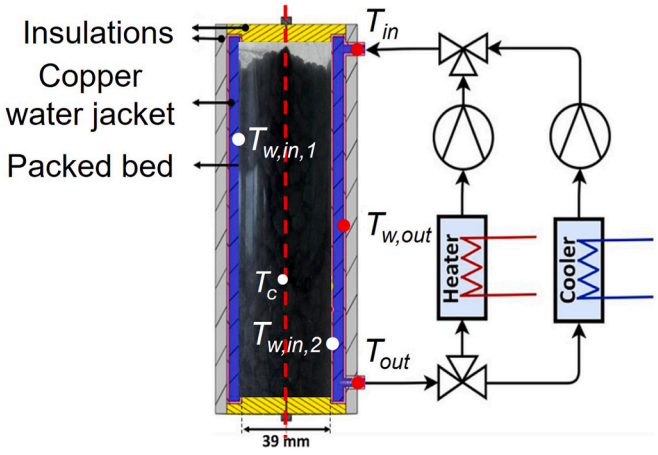

Fig. 4. Schematic illustration of experimental setup from (Rodrigues et al., 2022) used for ETC estimation of biochar packed beds. Temperature measurement points: T_{in} and T_{out}, at the inlet and outlet of heat transfer fluid (water) to the double jacket; $T_{w,in,1}$ and $T_{w,in,2}$, inner wall of the double jacket; $T_{w,out}$, outer wall of the cylinder; T_c, centerline of the packed bed.

insulated to the sides. The face insulations are used to promote the one-dimensionality of the temperature field and the applicability of the respective analytical solution. In more details, the setup reflects the case of an infinitely long cylinder, for which it can be anticipated that heat is transferred only in radial direction (Avila-Acevedo & Tsotsas, 2008; Rodrigues et al., 2023). Because of high water flow rates, the boundary conditions are close to a boundary condition of the first kind and axial temperature gradients do not occur.

The particles were weighed before being filled into the cylinder. The filling procedure was realized by several subsequent filling and tapping steps. The final bed height after this procedure was 11-14 cm in all experiments.

From the height of the bed and the bed mass, the bed density in Eq. (8) was calculated in order to determine the packed bed porosity. For this purpose, we filled a transparent cylinder with exactly the same geometry as the copper cylinder used for ETC estimation. Note that care was taken so that the particle bed surface was flat before height measurement. Tapping of the particle bed had only a slight impact on porosity and ETC. Repeatability was ensured by 3 times tapping.

The cylinder was first tempered at 22 °C and then cooled down to 15 °C by water flowing with a rate of 21 l/min through its double jacket. The large flow rate ensured that the temperatures of the water jacket and the inner wall were nearly constant in space and remained very close to each other.

The inner wall temperature, $T_{w,in}$, was determined from the average values of $T_{w,in,1}$ and $T_{w,in,2}$ while the bed center temperature, T_c, was detected with a thermocouple that was centrally inserted into the packing. Once the wall temperature was set to 15 °C the thermal response at the bed center, T_c, was monitored for estimation of ETC.

This experimental setup simulates transient heat conduction in an infinitely long cylinder with first-kind thermal boundary condition (i.e. constant wall temperature). Convective heat transfer by air is disregarded in this approach (Avila-Acevedo & Tsotsas, 2008). This assumption is valid only when the water jacket and cylinder wall can be regarded as isothermal, which was controlled by the axially distributed temperature measurements.

The reduced effective or bed thermal conductivity (reduced ETC) is calculated by the ratio of bed thermal conductivity (ETC) to gas thermal conductivity:

$$k_b[-] = \frac{\lambda_b}{\lambda_g} \tag{14}$$

The ETC, λ_b, was determined from the temperature response of T_c recorded during cooling of the particle bed following the procedure described in (Avila-Acevedo & Tsotsas, 2008; Rodrigues et al., 2022), i. e., by fitting λ_b in the equations below to the experimental data:

$$\theta = \frac{T_c - T_w}{T_{c,i} - T_w} = \frac{2}{\lambda_n} \sum_{n=1}^{\infty} \frac{e^{-\lambda_n{}^2 \tau}}{J(\lambda_n)}, \tag{15}$$

(Avila-Acevedo & Tsotsas, 2008; Tsotsas, 2010) with dimensionless temperature θ, current center temperature T_c, initial center temperature $T_{c,i}$, wall temperature T_w and first order Bessel function $J(\lambda_n)$. In this, λ_n are the roots of equation $J(\lambda_n) = 0$. Furthermore:

$$\tau = \frac{\alpha_b t}{R^2}, \tag{16}$$

with time t, inner cylinder radius $R = 19.5$ mm and

$$\alpha_b = \frac{\lambda_b}{(\rho c_p)_b}. \tag{17}$$

In this:

$$(\rho c_p)_b = \varepsilon_b \rho_g c_{p,g} + (1 - \varepsilon_b) \rho_p c_{p,p}. \tag{18}$$

The solution of Eq. (18) requires the specific heat capacity $c_{p,p}$, Eq. (13), and density ρ_p, Eq. (5), of the particles as well as void fraction ε_b, Eqs. (8) and (10), of the particle bed. Note that the intra-particle void fraction within the particles is not regarded here but considered as a contribution to the (effective) single particle properties.

For each biochar sample (MDP1 to MDP5), measurement and evaluation of ETC were repeated with two packings with the same sample material. Additionally, measurements were repeated 3 times with each packing to ensure repeatability of the results.

2.7. Literature models and extended ZBS

Relevant literature models are often categorized into three groups (Tsotsas, 2010; Tsotsas & Martin, 1987a): Type I models, with precise analytical or numerical calculation of the temperature field; type II models, which are basically resistance combination methods; type III models, incorporating unit cell approaches and further divided into group IIIa, assuming parallel heat flux lines, and group IIIb, assuming parallel isotherms.

Type I models are based on the solution of the Laplace equation for heat conduction. The earliest and simplest solution was introduced by Maxwell (1873). Two cases are further differentiated: Maxwell model with particle inclusions (Tsotsas, 2010),

$$\lambda_{sparse} = \lambda_g \cdot \frac{2\lambda_g + \lambda_p + 2(1 - \varepsilon_b)(\lambda_p - \lambda_g)}{2\lambda_g + \lambda_p - (1 - \varepsilon_b)(\lambda_p - \lambda_g)}, \tag{19}$$

and the Maxwell model with gas inclusions (Tsotsas, 2010):

$$\lambda_{dense} = \lambda_p \cdot \frac{2\lambda_p + \lambda_g + 2\varepsilon_b(\lambda_g - \lambda_p)}{2\lambda_p + \lambda_g - \varepsilon_b(\lambda_g - \lambda_p)}. \tag{20}$$

These two approaches average the structural bed properties by either assuming a sparse packing, with dominance of inter-particle voids, Eq. (19), or a dense packing with a greater impact of the particle's thermal conductivity, Eq. (20).

Type II models differentiate the thermal resistance associated with conduction through the solid and fluid phases: The parallel model (Tsotsas, 2010),

$$\lambda_{para} = \varepsilon_b \lambda_g + (1 - \varepsilon_b) \lambda_p, \tag{21}$$

serves generally as an orientation for the upper limit of ETC, whereas the series model (Tsotsas, 2010),

$$\lambda_{series} = \left[\frac{\varepsilon_p}{\lambda_g} + \frac{(1 - \varepsilon_p)}{\lambda_p} \right]^{-1}, \tag{22}$$

provides the lower limit of thermal conductivity. Both relationships depend on the assumption of a preferred direction of heat transfer: Either in parallel to the solid (i.e. the component with the higher thermal conductivity) or perpendicular to its orientation. The two cases thus represent the theoretical limits of heat transfer. Since the bed structure is rather isotropic in this study, heat transfer is supposed to occur in parallel and in series connection of the solid as well.

In type III models, a unit cell with the same ETC as the packed bed is considered. Type III models are often recommended for practical applications, particularly the model developed by Zehner, Bauer, and Schlünder (ZBS).

In the version of the ZBS model that has been presented by Rodrigues et al. (2023), the reduced ETC is computed from:

$$k_b = \left(-\Psi_{3D}{}^m + \frac{\varepsilon_b{}^{(n-1)}}{(1 - \sqrt{1 - \varepsilon_b})^n} \right)^{-1} \cdot \varepsilon_b \cdot \left(\varepsilon_b - 1 + \frac{1}{k_g} \right)^{-1} + \sqrt{1 - \varepsilon_b} \cdot \left(\varphi k_p + (1 - \varphi) k_c \right), \tag{23}$$

with empirical constants $m = 8.8788$ and $n = 1.0534$. Eq. (23) assumes that the (local) porosity of the unit cell is equal to the (macroscopic) bed

Table 2
Parameters used in Eqs. (23) and (27).

Name	Equation	Unit
Reduced thermal conductivity of core region	$k_c = \frac{\lambda_c}{\lambda_g} = \frac{2}{N} \left(\frac{B}{N^2} \frac{k_p - 1}{k_p k_g} \cdot \ln\left(\frac{k_p}{B \cdot (k_g + (1 - k_g) k_p)} \right) - \frac{B+1}{2} - \frac{(B-1)}{N k_g} \right)$	-
Geometry configuration parameter	$N = \frac{1}{k_g} \left(1 - \frac{B k_g}{k_p} \right) - B \left(\frac{1}{k_g} - 1 \right)$	-
Deformation parameter	$B = C_f \left(\frac{1 - \varepsilon_b}{\varepsilon_b} \right)^{\frac{10}{9}}$	-
Shape factor	$C_f = 6.557 \cdot \Psi_{3D} + 3.184$	-
Flattening coefficient	$\varphi = -0.4689 \cdot \Psi_{3D} + 0.4656$	-
Reduced gas conductivity	$k_g = \left[1 + \frac{l}{d_{pv}} \right]^{-1}$	-
Modified mean free path of air molecules	$l = 2 \left(\frac{2 - \gamma}{\gamma} \right) \sqrt{\frac{2\pi \tilde{R} T}{\tilde{M}}} \frac{\lambda_g}{P \left(2 c_{p,g} - \frac{\tilde{R}}{\tilde{M}} \right)}$	m
Accommodation coefficient	$\ln\left(\frac{1}{\gamma} - 1 \right) = 0.6 - \frac{\frac{1000}{T} + 1}{2.8}$	-
Reduced particle conductivity	$k_p = \frac{\lambda_p}{\lambda_g}$	-

porosity, ε_b.

The calculation of the parameters contained therein is set out in Table 2 using the notation from (Rodrigues et al., 2023) and ideal gas constant, $\tilde{R} = 8314$ J/kmol/K, mean temperature in experiments, $T = 291.65$ K, molar mass of air, $\tilde{M} = 28.96$ kmol/kg, ambient pressure, $P = 101{,}325$ Pa, heat capacity of the gas phase, $c_{p,g} = 1005$ J/kg/K, and gas thermal conductivity, $\lambda_g = 0.025$ W/m/K.

In this approach, d_{pv} is the diameter of the volume equivalent sphere of the non-spherical particle. Note that the volume equivalent diameter was not determined in this study. Particle size distributions are based on the area equivalent diameter, d_A, as well as the length of the smallest lateral extension ($d_{\min}$) and the length of the largest lateral extension ($d_{\max}$) (cf. Section 3.1.1). We therefore used $d_{pv} = d_A$, potentially underestimating the particle diameter in this approach. The expected slight variation of d_{pv} though has only a marginal impact on k_g in Table 2, especially in the studied situation where the Knudsen effect plays a negligible role.

According to Rodrigues et al. (2023), Eq. (23) and the Maxwell model with gas inclusion (Maxwell dense) yield roughly similar values for spheres in case of a major contribution of thermal conduction along the particle contact points.

Here, however, sparse contact between solid particles is anticipated and a major contribution of heat conduction through the gas phase expected. This assumption is supported by XMT analyses and images in Figs. 1 and 3, where the actual thermal contact between particles appears much smaller than the apparent geometric contact surface.

Accordingly, we replaced k_p by the reduced thermal core conductivity as suggested in Rodrigues et al. (2022),

$$\frac{1}{k_{con}} = \frac{1}{k_p} + s^* + Kn. \tag{24}$$

In this,

$$Kn = \frac{l}{d_{pv}}, \tag{25}$$

and

$$s^* = \frac{s}{d_p}. \tag{26}$$

With this, we account for the significant contribution of heat transfer via the gas phase in the gap between particle interfaces as a consequence of the imperfect contact between them. Eq. (23) then reads:

$$k_b^{s*} = \left(-\Psi_{3D}{}^m + \frac{\varepsilon_b{}^{(n-1)}}{\left(1-\sqrt{1-\varepsilon_b}\right)^n} \right)^{-1} \cdot \varepsilon_b \cdot \left(\varepsilon_b - 1 + \frac{1}{k_g} \right)^{-1} + \sqrt{1-\varepsilon_b} \cdot (\varphi k_{con} + (1-\varphi) k_c), \tag{27}$$

and determines the reduced ETC of the packed bed, corrected by the gas-phase transport. The respective notation is $\mathrm{ETC}^{\mathrm{ZBS-E}}$, in which the upper index ZBS-E accounts for the extended Zehner-Bauer-Schlünder model.

Table 3
Summary of particle sizes and sphericity. Median particle diameter (d_A) is the diameter of the area-equivalent circle of the 2D projection from Camsizer at 50 % of the cumulative distribution (cf. Supplementary material, Fig. S1). Mode of 3D sphericity is the peak position of the probability function (cf. Supplementary material, Fig. S2). Median of 2D sphericity is the sphericity calculated by Eq. (2) at 50 % of the cumulative distribution.

Sample ID	Median of particle diameter d_A [mm]	Mode of 3D sphericity, Ψ_{3D} [-]	Median of 2D sphericity, Ψ_{2D} [-]
MDP1	0.42	0.68	0.89
MDP2	0.53	0.74	0.88
MDP3	1.83	0.72	0.81
MDP4	3.1	0.72	0.82
MDP5	5.0	0.69	0.78

The reduced ETC calculated using this equation is compared below with the experimentally determined reduced ETC values (Section 3).

3. Results and discussions

3.1. Particle properties

3.1.1. Particle size and sphericity

Table 3 summarizes experimental results. As can be seen, the mode value of volume sphericity obtained by XMT varies only slightly despite the variation in particle size distribution. The median values from the Camsizer instead suggest that the sphericity becomes larger, from $\Psi_{2D} = 0.78$ (MDP5) to 0.89 (MDP1), with decreasing particle sizes. However, the different trends might be rather based on individual uncertainties of the methods: In the imaging approach, the ratio between particle size and voxel size becomes smaller with decreasing particle size, which affects the determination of the particle surface area and volume. Deviations are thus more likely addressed to the small particle fractions. In the 2D projection, minor deviations in shape in the small particle fraction are not resolved, and the projected areas appear more spherical than the illuminated particle. This effect might explain the sphericity trend seen for Ψ_{2D} in the table.

3.1.2. Thermophysical properties

The thermophysical properties of the particle fractions are summarized in Table 4 together with the particle porosity. Note that it is expected that these properties are independent of the particle size, wherefore they were determined from extruded biochar prior to being crushed into smaller particles, as described in Section 2.1. The average envelope density, determined from the geometry and mass of the extruded cylindrical biochar pellets out of ten measurements, was $\rho_p = 686$ kg/m^3. The solid or skeleton density was computed from a sample volume of $V_s = 0.8307$ ml and a sample mass of $m_s = 1.7455$ g and is $\rho_s = 2101.3$ kg/m^3.

The experimentally estimated thermal conductivity of the biochar particles is $\lambda_p = 0.231 \pm 0.028$ W/m/K (LFA, Eq. (12)). This is significantly higher than the thermal conductivity of untreated pyrolyzed biomass, which was additionally measured and is 0.06 W/m/K. The data presented here was measured at 25 °C and the data from wider ranges of temperature (25-1000 °C) are presented in supplement material (Supplementary material, Fig. S3).

3.2. Packed bed properties

The particle bed properties, namely the inter-particle porosity, ε_b, Eqs. (8) and (10), and the overall porosity, ε_t, Eq. (11), are summarized in Table 5.

It is important to note that the values of ε_t in Table 5 are based on the sample holder used for ETC measurements (Fig. 4). In contrast, ε_b was obtained in two different ways: From the density estimated with the sample holder in Fig. 4 as well as from XMT data using a significantly smaller sample holder. In a smaller sample holder, packing and tapping (even with the same method) potentially result in different bed properties compared to results obtainable with the experimental setup in this

Table 4
Thermophysical properties of biochar particles at the given temperatures. The measurement of specific heat capacity and thermal conductivity were repeated with five samples where measurement was repeated three times for each sample.

Particle property	Property unit	Value
(Intra-) Particle porosity, ε_p (Eq. (7))	-	0.67
Envelope density (at 20 °C), ρ_p	kg/m^3	686
Solid (skeleton) density (at 20 °C), ρ_s	kg/m^3	2101
Specific heat capacity (at 25 °C), $c_{p,p}$	J/kg/K	610 ± 57
Thermal conductivity (at 25 °C), λ_p	W/m/K	0.231 ± 0.028

Table 5
Porosities of the packed beds.

Property	Unit	MDP1	MDP2	MDP3	MDP4	MDP5
(Inter-) Particle porosity, ε_b (Eq. (8))	-	0.34	0.37	0.31	0.31	0.48
(Inter-) Particle porosity, ε_b^{3D} (Eq. (10))	-	0.39	0.35	0.43	0.47	0.47
Bed porosity, ε_t (Eq. (11))	-	0.78	0.79	0.77	0.77	0.83

figure, especially if the sample holder diameter is much smaller. This explains the different values in the table. As can be seen, XMT measurements yielded in most cases slightly different porosity values than estimation with the setup in this figure. For the later evaluation of ETC (Section 3.3), we will refer to the values obtained by Eq. (8) because they are referred to the very same setup as the ETC measurements. Nevertheless, porosity is higher for larger particles (MDP5), as the ratio between cylinder diameter, D, and particle diameter, d_A, is $D/d_A < 20$. In consequence, a generally lower ETC can be expected for MDP5 than would be the case if porosity would be lower.

3.3. Experimental ETC results

The reduced ETC, Eq. (14), was experimentally derived at room temperature using the method from Section 2.6. The thermodynamic and structural properties of the different particle fractions used in the estimation are summarized in Table 6. The inter-particle porosity was computed from Eq. (8), Tables 5, i.e. using the experimental data obtained with the experimental setup also used for the ETC measurements. The gas properties used in Eqs. (14)–(18) are the specific air thermal conductivity, y $\lambda_g = 0.025$ W/m/K, the gas density, $\rho_g = 1.204$ kg/m^3, the heat capacity, $c_{p,g} = 1005$ J/kg/K and $(\rho c_p)_g = 1210.02$ J/m^3/K. The particle properties are the envelope particle density, $\rho_p = 686$ kg/m^3 (Eq. (5)), heat capacity at 25 °C, $c_{p,p} = 610$ J/kg/K and $(\rho c_p)_p = 418{,}460$ J/m^3/K.

Fig. 5(a) presents the k_b values from Table 6 as function of the median of the particle diameter, d_A, from Table 3; Fig. 5(b) presents additionally k_b as function of inter-particle porosity, ε_b, Eq. (8). In both plots, the experimentally observed variation is provided as of minimum, maximum and mean values by error bars.

Fig. 5 clearly reveals that k_b varies only slightly in the studied ranges of particle diameter and bed porosity. More precisely, it decreases from around 3 to roughly 2.5 with increasing particle size and porosity. It is likely that the estimated porosity of MDP5 (Table 6) is affected by the relatively small D/d_A ratio of ca. 8, which may have contributed to an influence of the wall effect. For higher D/d_A ratios, a lower porosity would be expected, potentially yielding a higher ETC of MDP5 as well.

With this in mind, the ETC of the studied densified biochar is barely sensitive to porosity and particle size, being in line with literature for non-spherical particles with low particle conductivity (Rodrigues et al., 2023). For particle to gas conductivity ratios of $k_b < 40$, literature reports rather independence of ETC on particle shape and size. Our k_b value for irregular particles is on average 2.91, i.e. much lower than the critical value reported in Rodrigues et al. (2023).

As the ETC determination strongly depends on the accuracy of Eq. (18), i.e. accurate particle density and heat capacity as well as packed bed porosity, Table 7 provides data as a basis for sensitivity evaluation. In this, the computed values are provided for ± 10 % variation. This shows that the reduced ETC of MDP5 could be increased to values in the range of MDP1 to MDP4 already for a variation of Eq. (18) of ± 10 %, e.g. induced by porosity variation.

3.4. Numerical assessment of experimental data

The literature models, Eqs. (19)–(22) were solved with $\lambda_p = 0.231$ W/m/K from Table 4 and $\lambda_g = 0.025$ W/m/K. Porosity, ε_b, was varied between 0 and 1. The results are presented in Fig. 6(a).

Application of Eq. (19) to packed beds of spherical particles usually provides reliable results when $\lambda_p/\lambda_g < 20$, which is also fulfilled in this study. It is therefore not surprising that the experimental data are found at the lower end of theoretical ETC, i.e. between the series model and Maxwell-sparse, Eq. (19). This suggests that individual particles exert a rather weak thermal influence on each other.

The ZBS-E model with $s^* = 0$, Eq. (23), is expected to yield ETC values greater than the Maxwell-sparse model. Fig. 6(a) shows that introduction of a positive s^*, Eq. (27) in the ZBS-E model, accounting for imperfect thermal connection of biochar particles, can achieve similar values as Maxwell-sparse. Eq. (27) was solved with $s^* = 0.25$, i.e. when the distance between the particles corresponds to a quarter of the particle size. In fact, in Eq. (24), $s^* = 0.25$ is 1.6 times larger than $1/k_p$, being 0.1546, and Kn $\ll 1$. This shows that the resistance inside of the imperfect contact region between particle surfaces significantly contributes to $1/k_{con}$. The contact area ratio, $\varphi = 0.12$ to 0.15, is relatively large and comparable to pyramids or triangular prisms (Rodrigues et al., 2023). However, with s^* being greater than 0, the dispersed particles appear to have no significant thermal contact area.

Note that smaller values of s^* would increase ETC^{ZBS-E}, yielding similar values as Eq. (23). Larger values instead would only slightly affect the ETC^{ZBS-E}. It is therefore not possible to fit ETC^{ZBS-E} exactly to the experimental values. Due to the low sensitivity of the ETC on structural parameters for particles with low thermal conductivity it is furthermore not possible to achieve a better fit based on a variation of geometrical parameters.

A better agreement of our experimental measurement and ZBS-E/Maxwell-sparse is only obtained, if the particle conductivity is reduced. For the plots in Fig. 6(a), the value from Table 4 ($\lambda_p = 0.231$ W/m/K), i.e. experimentally obtained by LFA, was used. In Fig. 6(b), model equations from Section 2.7 were solved with a slightly smaller λ_p of 0.1617 W/m/K, yielding a good agreement between reduced ETC values from experiments and ZBS-E/Maxwell-sparse. This finding can be explained from two perspectives. On the one hand, the experimental ETC could have been slightly underestimated due to uncertainties in the measurement, especially in the exact temperature detection. But, also density and heat capacity of the solid are included in respective calculations, Eqs. (14)–(18), contributing with their own measurement (in) accuracy. This is reflected by the error bar of experimental data in Fig. 6. On the other hand, uncertainties related to the impact of surface roughness in the LFA measurement might have yielded too high values of the particle's thermal conductivity. Eq. (12) is calculated from the thickness and cross-sectional area of the sample. Even though great care has been taken to obtain a smooth sample surface, it inheritably contains

Table 6
Summary of parameters used for ETC calculations, Eqs. (14)–(18) and experimentally determined ETC of each particle fraction. Thermo-physical properties were measured at 25 °C. The ETC measurement was realized between 15 and 22 °C. Measurement and evaluation of ETC were repeated with two packings with the same sample material and each measurement repeated 3 times with each packing. The estimated standard deviation is provided along with the ETC value.

Property	Property unit	MDP1	MDP2	MDP3	MDP4	MDP5
Inter-Particle Porosity, ε_b (Eq. (8))	-	0.34	0.37	0.31	0.31	0.48
$(\rho c_p)_b$ (Eq. (18))	J/m^3/K	277x10^3	265x10^3	291x10^3	290x10^3	220x10^3
ETC of the packed bed, λ_b	W/m/K	0.0745	0.0745	0.0767	0.0748	0.0633
Reduced ETC, k_b (Eq. (14))	-	2.98 ± 0.13	2.98 ± 0.13	3.07 ± 0	2.99 ± 0.10	2.53 ± 0

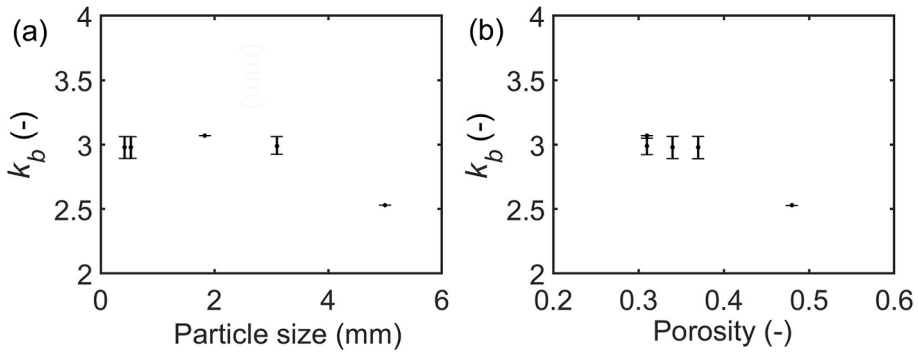

Fig. 5. Reduced ETC, k_b, with respect to (a) median of the particle diameter, d_A, from Table 3, and (b) the inter-particle porosity, ε_b, based on the same experimental setup and Eq. (8). Measurement and evaluation were repeated with two packings with the same sample material and each measurement repeated 3 times with each packing. The minimum and maximum values are indicated by the error bars together with the mean ETC value (point).

Table 7
Sensitivity study of reduced ETC, k_b. Uncertainty of ± 10 % is introduced in $(\rho c_p)_b$ from Eq. (18).

Sample ID	k_b from Table 6 [-]	k_b for $(\rho c_p)_b$ x 1.1 [-]	k_b for $(\rho c_p)_b$ x 0.9 [-]
MDP1	2.98 ± 0.13	2.68 ± 0.042	3.33 ± 0.13
MDP2	2.98 ± 0.13	2.68 ± 0.042	3.24 ± 0.17
MDP3	3.07 ± 0	2.71 ± 0	3.33 ± 0.13
MDP4	2.99 ± 0.10	2.80 ± 0.13	3.33 ± 0.13
MDP5	2.53 ± 0	2.36 ± 0	2.89 ± 0

sub-mm roughness due to the fact that densified char consists of the binded biochar grains (which themselves are 0.1−1 mm in size). The sample thickness was measured with calipers. Hence, there is a certain possibility to yield higher density with the LFA method, which may consequently result in apparently higher ETC values.

Maxwell-sparse and ZBS-E in Fig. 6(b) were both solved with constant values of λ_p (and s^* in ZBS-E). It would have been possible to fit all points to the exact experimental values by adjusting λ_p and s^* individually for each case. This would, though, have impaired the universality of the approach. The remaining deviations might be rather associated to measurement uncertainties, related either to the method from Section 2.6 and/or additionally to the determination of particle size, sphericity and porosity.

ZBS-E and Maxwell-sparse both clearly show a dependence on porosity. The same trend can be expected from the ETC measurements if all inaccuracies could be avoided. A reduction in porosity through structural adaptation is therefore capable of increasing ETC, even in presence of the thermal contact resistance. A similar conclusion could be drawn for alteration of the thermal conductivity of particles. The comparison of the two graphs in Fig. 6 shows that tailoring λ_p has an impact on the reduced ETC, that is, higher λ_p can increase ETC of the biochar packed bed. These findings are in agreement with results reported in Rodrigues et al. (2022).

It should be noted that all the experimental and modeling data presented in this study are obtained at 25 °C. This temperature range is relevant to the biochar storage conditions where the occurrence of self-heating is becoming a serious issue. The ETC from this study can be directly applied to estimate the degree of self-heating through the competition among exothermic chemisorption of O_2, heat dissipation, and O_2 diffusion through the packed bed.

However, the applicability of the ZBS model in wider temperature ranges is its particular advantage. Especially highlighted are processes at higher temperatures, as e.g. occurring in metallurgical processes. In this, ZBS can account for radiation (cf. Rodrigues et al., 2023; Tsotsas, 2010; Tsotsas & Martin, 1987b) with certain limitations, i.e. radiation over more than one particle layer is neglected and only layer-to-layer radiation is considered. The variation of particle contacts in such cases, e.g. growth by melting at high temperatures, can be accounted for by the flattening coefficient. In brief, application of the model to larger temperature ranges requires additional information. This includes additionally the change of thermo-physical properties of particles and gas (Rodrigues et al., 2023; Tsotsas, 2010; Tsotsas & Martin, 1987b). Particle thermal conductivity and heat capacity at wider temperature ranges (25–1000 °C) is therefore presented in the dataset publication (Vorhauer-Huget et al., 2026) and in the supplementary material (Fig. S3).

4. Conclusions

This work investigated the effective thermal conductivity of packed beds of irregularly shaped pyrolyzed and densified biochar particles in

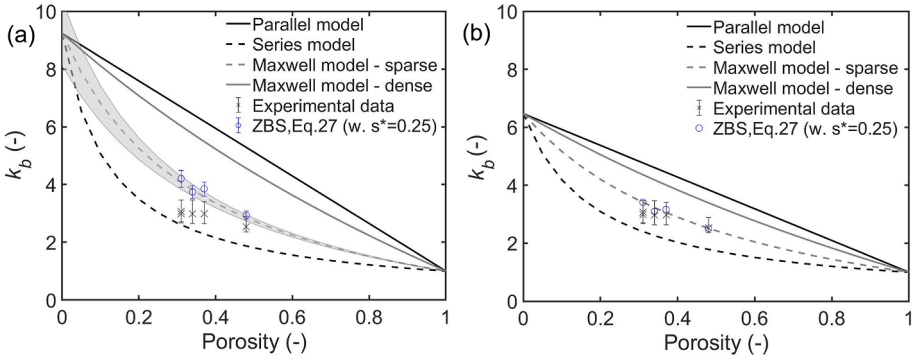

Fig. 6. (a) Comparison of experimental data from this work to the solutions of analytical models in the literature using experimentally obtained particle thermal conductivity by LFA (i.e. $\lambda_p = 0.231$ W/m/K). The error bars in experimental data are based on ± 10 % uncertainty of $(\rho c_p)_b$. Shaded areas for Maxwell model (sparse) and the error bars for ZBS model represent the propagated uncertainties of the LFA measurement in particle thermal conductivity. (b) Best fit of ZBS-E, Eq. (27) and Maxwell-sparse, Eq. (19) models to experimental data. Particle thermal conductivity was used as the fitting parameter and the best fit was obtained with $\lambda_p = 0.1617$ W/m/K.

stagnant air. A combination of experimental techniques together with numerical analysis was used to characterize both, particle-scale and bed-scale properties, including density, porosity, specific heat capacity, and thermal conductivity.

The reduced experimental ETC, $k_b = \lambda_b/\lambda_g$, was found in the range between 2.5 and 3.1 (corresponding to $\lambda_b = 0.0625$ to 0.0775 W/m/K), being in good agreement with predictions by the Maxwell-sparse model as well as the ZBS-E model from Rodrigues et al. (2022, 2023), using a particle thermal conductivity of $\lambda_p = 0.1617$ W/m/K in computations. The reversely estimated λ_p from the models is slightly smaller than the value determined by Laser Flash Analysis, which could have several reasons, as discussed.

ETC of porous biochar particles follows the same dependency on porosity as Maxwell-sparse in the studied range of moderate bed porosity. Additional numerical analysis with the extended ZBS-E model (Rodrigues et al., 2022, 2023) revealed quantitative details about the thermal resistance between single particles. Despite the relatively large contact area ratio, φ, of 0.12 to 0.15, being comparable to that of pyramids or triangular prisms (Rodrigues et al., 2023), the dispersed particles appeared to have no significant thermal contact area. This finding was supported by XMT images, which showed only rare contacts between single particles. The low ETC of 2.5 to 3.1 was therefore not only associated to the low λ_p of porous biochar particles, but also the thermal resistance in the particle contact area was identified to play a significant role.

The combination of the ZBS-E model analysis and experimental determination provided a sound base for the interpretation of ETC results obtained for the densified biochar that would otherwise not have been possible with Maxwell-sparse or experiments alone. Especially, the gained understanding of the impact of the thermal resistance in the gas-gap between particles is an important factor in improving thermal processes with porous biochar particles, as e.g. storage or thermal insulation.

CRediT authorship contribution statement

Nicole Vorhauer-Huget: Writing – review & editing, Validation, Supervision, Resources, Project administration, Methodology, Investigation, Funding acquisition, Formal analysis, Conceptualization. **Zahra Ghasemi Monfared:** Writing – original draft, Visualization, Methodology, Investigation, Data curation, Conceptualization. **Neda Kazemi:** Software, Methodology, Data curation. **Eduardo Arango Durango:** Methodology, Data curation. **Evangelos Tsotsas:** Writing – review & editing, Validation, Supervision, Resources, Project administration, Methodology, Funding acquisition, Formal analysis, Conceptualization. **Kentaro Umeki:** Writing – review & editing, Validation, Supervision, Resources, Project administration, Methodology, Investigation, Funding acquisition, Formal analysis, Data curation, Conceptualization.

Declaration of competing interest

The authors declare that they have no known competing financial interests or personal relationships that could have appeared to influence the work reported in this paper.

Acknowledgements

The authors N. Vorhauer-Huget, N. Kazemi and E. Tsotsas acknowledge the funding by the Deutsche Forschungsgemeinschaft (DFG, German Research Foundation) – Project-ID 422037413 – TRR 287 for their contributions to the study.

Z. Ghasemi Monfared, E. Arango Durango and K. Umeki acknowledge the funding by the Swedish Energy Agency (Project number: P46974-1), part of which is funded by The Recovery and Resilience Facility, RRF of European Commission (EU), and Swedish Research Council (Project number: 2023-04185). We express our gratitude to Henrik Lycksam for the XMT-scans.

Appendix A. Supplementary data

Supplementary data to this article can be found online at https://doi.org/10.1016/j.partic.2026.06.036.

Data availability

The underlying research data required to reproduce these findings are openly available in the Zenodo repository (https://doi.org/10.5281/zenodo.20660734) and at Swedish National Data Service (https://doi.org/10.5878/pgq2-ga70).

References

Avila-Acevedo, J. G., & Tsotsas, E. (2008). Transient natural convection and heat transfer during the storage of granular media. *International Journal of Heat and Mass Transfer, 51*, 3468–3477. https://doi.org/10.1016/j.ijheatmasstransfer.2007.10.035

Babler, M. U., Phounglamcheik, A., Amovic, M., Ljunggren, R., & Engvall, K. (2017). Modeling and pilot plant runs of slow biomass pyrolysis in a rotary kiln. *Applied Energy, 207*, 123–133. https://doi.org/10.1016/j.apenergy.2017.06.034

Bianchi Janetti, M., Krusharova, M., Fend, F., Längle, K., & Mathis, T. (2024). Thermal conductivity of biochar-clay composites for the internal insulation of buildings. *Case Studies in Construction Materials, 21*, Article e04083. https://doi.org/10.1016/j.cscm.2024.e04083

Cheng, G. J., Yu, A. B., & Zulli, P. (1999). Evaluation of effective thermal conductivity from the structure of a packed bed. *Chemical Engineering Science, 54*(19), 4199–4209. https://doi.org/10.1016/S0009-2509(99)00125-6

Gan, J., Zhou, Z., & Yu, A. (2017). Effect of particle shape and size on effective thermal conductivity of packed beds. *Powder Technology, 311*, 157–166. https://doi.org/10.1016/j.powtec.2017.01.024

Govender, N., Cleary, P. W., Kiani-Oshtorjani, M., Wilke, D. N., Wu, C. Y., & Kureck, H. (2020). The effect of particle shape on the packed bed effective thermal conductivity based on DEM with polyhedral particles on the GPU. *Chemical Engineering Science, 219*. https://doi.org/10.1016/j.ces.2020.115584

Hamilton, R. L. (1962). Thermal conductivity of heterogeneous two-component systems. *Industrial and Engineering Chemistry Fundamentals, 1*, 187–191. https://doi.org/10.1021/i160003a005

Khaledi, S., Delbari, M., Galavi, H., Bagheri, H., & Chari, M. M. (2023). Effects of biochar particle size, biochar application rate, and moisture content on thermal properties of an unsaturated sandy loam soil. *Soil and Tillage Research, 226*, Article 105579. https://doi.org/10.1016/j.still.2022.105579

Kiradjiev, K. B., Halvorsen, S. A., Van Gorder, R. A., & Howison, S. D. (2019). Maxwell-type models for the effective thermal conductivity of a porous material with radiative transfer in the voids. *International Journal of Thermal Sciences, 145*. https://doi.org/10.1016/j.ijthermalsci.2019.106009

Kunii, D., & Smith, J. M. (1960). Heat transfer characteristics of porous rocks. *AIChE Journal, 6*, 71–78. https://doi.org/10.1002/aic.690060115

Lindblad, J., & Nyström, I. (2002). Surface area estimation of digitized 3D objects using local computations. In A. Braquelaire, J. O. Lachaud, & A. Vialard (Eds.), *Lecture notes in computer science: 2301. Discrete geometry for computer imagery*. Berlin, Heidelberg: Springer. https://doi.org/10.1007/3-540-45986-3_24. DGCI.

Liu, S., Peng, S., Zhang, B., Xue, B., Yang, Z., Wang, S., & Xu, G. (2022). Effects of biochar pyrolysis temperature on thermal properties of polyethylene glycol/biochar composites as shape-stable biocomposite phase change materials. *RSC Advances, 12*, 9587–9598. https://doi.org/10.1039/D1RA09167K

Mason, P. E., Darvell, L. I., Jones, J. M., & Williams, A. (2016). Comparative study of the thermal conductivity of solid biomass fuels. *Energy Fuels, 30*, 2158–2163. https://doi.org/10.1021/acs.energyfuels.5b02261

Maxwell, J. C. (1873). *A treatise on electricity and magnetism*. Oxford: Clarendon Press.

Nasr, K., Viskanta, R., & Ramadhyani, S. (1994). An experimental evaluation of the effective thermal conductivities of packed beds at high temperatures. *Journal of Heat Transfer, 116*, 829–837. https://doi.org/10.1115/1.2911455

Object research systems, https://www.theobjects.com/company/index.html (accessed on September 15, 2022).

Osman, A. I., Farghali, M., Dong, Y., et al. (2024). Reducing the carbon footprint of buildings using biochar-based bricks and insulating materials: A review. *Environmental Chemistry Letters, 22*, 71–104. https://doi.org/10.1007/s10311-023-01662-7

Qian, Y., Han, Z., Zhan, J. H., Liu, X., & Xu, G. (2018). Comparative evaluation of heat conduction and radiation models for CFD simulation of heat transfer in packed beds. *International Journal of Heat and Mass Transfer, 127*, 573–584. https://doi.org/10.1016/j.ijheatmasstransfer.2018.06.127

Ramandi, H. L., Mostaghimi, P., Armstrong, R. T., Saadatfar, M., & Pinczewski, W. V. (2016). Porosity and permeability characterization of coal: A micro-computed tomography study. *International Journal of Coal Geology, 154–155*, 57–68. https://doi.org/10.1016/j.coal.2015.10.001

Redenbach, C., Ohser-Wiedemann, R., Löffler, R., Bernthaler, T., & Nagel, A. (2011). Characterization of powders using micro computed tomography. *Particle and Particle Systems Characterization, 28*, 3–12. https://doi.org/10.1002/ppsc.200900088

Rodrigues, S. J., Vorhauer-Huget, N., & Tsotsas, E. (2022). Effective thermal conductivity of packed beds made of cubical particles. *International Journal of Heat and Mass Transfer, 194*, Article 122994. https://doi.org/10.1016/j.ijheatmasstransfer.2022.122994

Rodrigues, S. J., Vorhauer-Huget, N., & Tsotsas, E. (2023). Prediction of effective thermal conductivity of packed beds of polyhedral particles. *Powder Technology, 430*. https://doi.org/10.1016/j.powtec.2023.118997

Thunman, H., & Leckner, B. (2002). Thermal conductivity of wood-models for different stages of combustion. *Biomass and Bioenergy, 23*(1), 47–54. https://doi.org/10.1016/S0961-9534(02)00031-4

Tsotsas, E. (2010). Thermal conductivity of packed beds. In *Section D6.3, VDI heat Atlas* (2nd ed.). Berlin: Springer, ISBN 978-3-540-77876-9.

Tsotsas, E., & Martin, H. (1987a). Thermal conductivity of packed beds: A review. *Chemical Engineering and Processing: Process Intensification, 22*(1), 19–37. https://doi.org/10.1016/0255-2701(87)80025-9

Tsotsas, E., & Martin, H. (1987b). Thermal conductivity of packed beds: A review. *Chemical Engineering and Processing, 22*, 19–37. https://doi.org/10.1016/0255-2701(87)80025-9

Tsotsas, E., & Schlünder, E.-U. (1990). Heat transfer in packed beds with fluid flow: Remarks on the meaning and the calculation of a heat transfer coefficient at the wall. *Chemical Engineering Science, 45*, 819–837. https://doi.org/10.1016/0009-2509(90)85005-X

Valverde, A., & Wijewickreme, D. (2024). Using x-ray micro CT imaging data to obtain particle morphology and soil fabric parameters. In *Proceedings of the E3S web of conferences, 544*EDP Sciences, Article 04008. https://doi.org/10.1051/e3sconf/202454404008.

Van Antwerpen, W., Du Toit, C. G., & Rousseau, P. G. (2010). A review of correlations to model the packing structure and effective thermal conductivity in packed beds of mono-sized spherical particles. *Nuclear Engineering and Design, 240*, 1803–1818. https://doi.org/10.1016/j.nucengdes.2010.03.009

Vorhauer-Huget, N., Ghasemi Monfared, Z., Kazemi, N., Arango Durango, E., Tsotsas, E., & Umeki, K. (2026). *Experimental data for computation of effective thermal conductivity of packed bed of porous biochar particles*. Zenodo. https://doi.org/10.5281/zenodo.20660734

Xu, J. Z., Gao, B. Z., & Kang, F. Y. (2016). A reconstruction of Maxwell model for effective thermal conductivity of composite materials. *Applied Thermal Engineering, 102*, 972–979. https://doi.org/10.1016/j.applthermaleng.2016.03.155

Zehner, P., & Schlünder, E. U. (1970). Wärmeleitfähigkeit von Schüttungen bei mäßigen Temperaturen. *Chemie Ingenieur Technik, 42*. https://doi.org/10.1002/cite.330421408